Table 1 Summary of improvement in fit with the three-compartment model over the two-compartment model

Study group	Number of curves	Mean AIC two-compartment	Mean AIC three-compartment	Mean SC two-compartment	Mean SC three-compartment	Number of curves (%) (three-compartment better than two-compartment)[a]
Resting	35	652.4	630.2 ($p<0.01$)	663.8	638.4 ($p<0.01$)	24 (69)
Beta-blocker	20	378.4	378.8 (p=n.s.)	382.0 ($p<0.01$)	384.7	3 (15)
Adenosine	45	405.1	393.6 ($p<0.01$)	408.7	399.5 ($p<0.01$)	28 (62)

The p value indicates that the value in the cell is significantly lower than the corresponding other value.
AIC: Akaike information criterion, *SC*: Schwarz criterion
[a] This column gives the number of TTAC fits where the three-compartment model fit provided a significant improvement over the two-compartment fit according to all criteria (AIC, SC).

AIC and SC demonstrated that the three-compartment model fit provided significant improvement over the two-compartment model fit for resting and adenosine studies. For the beta-blocker studies, AIC between the two model fits was not significantly different, whilst SC demonstrated significantly better fit with the two-compartment model. Improved AIC and SC for the three-compartment model fit were observed in 69% of resting TTACs and 62% of adenosine TTACs, but only 15% in beta-blocker TTACs.

As shown in Fig. 7a and b, the K_1 and V_d values derived from the two-compartment model fit showed significant differences compared with those by the three-compartment model. Both K_1 and V_d were under-estimated with the two-compartment model fit compared with the three-compartment model fit. It should, however, be noted that there was a good correlation between the two- and three-compartment models for K_1, thus the bias introduced by the two-compartment model fit can potentially be corrected. K_1 values by the three-compartment model fit with all three corrections were 0.86±0.36, 2.71±1.64 and 0.55±0.24 ml/min/g corresponding to rest, adenosine infusion (with constant infusion at 140–700 mg/kg/h) and beta-blocker (with 2–6 mg administration), respectively. Difference in V_d was less than 10% and again this bias can potentially be corrected by the regression equation. The K_1 obtained with the two-compartment model also demonstrated a good correlation with the microsphere flow (Fig. 7c), though there was again a systematic under-estimation in K_1.

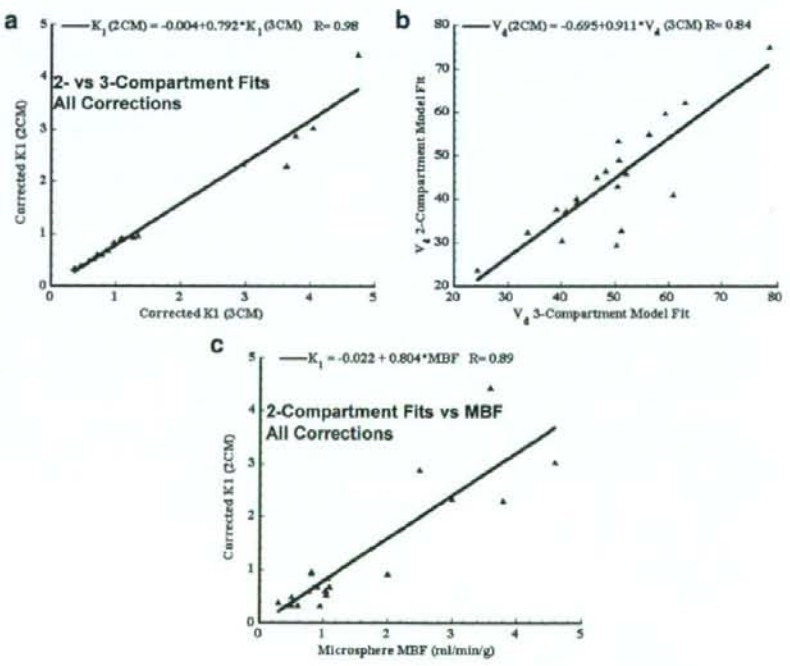

Fig. 7 **a** Plot of K_1 estimates derived from the two-compartment model fit against those from the three-compartment model fit. **b** Plot of V_d estimates derived from the two-compartment model fit against those from the three-compartment model fit. **c** Plot of K_1 values derived from the two-compartment model fit against mean of the pre- and post-dynamic SPECT microsphere blood flow measurements

amplification. Curve fits to representative TTACs for resting, beta-blocker and adenosine infusion studies are shown in Fig. 5. The height of the TTACs relative to the input function corresponded well with the pharmacological challenges. Compared to the resting studies, peaks of TTACs relative to the arterial input function were higher for adenosine and lower after beta-blocker administration. Results of kinetic fitting by the two- and three-compartment models are also plotted on this figure. Visually, the three-compartment model provided better fits than the two-compartment model to the observed TTACs, which is particularly evident for the initial scan period of the resting and adenosine studies.

Shown in Fig. 6a–e is the comparisons of K_1 obtained by NLLSF (three-compartment model fit) with the microsphere flow estimates. Values were averaged over the myocardial segments in both axes, thus each point corresponds to a single study. There was good correlation between K_1 and the microsphere flow when no corrections were applied, but K_1 significantly under-estimated the true flow (Fig. 6a). All the corrections improved the K_1 estimates (Fig. 6b–d) and the best agreement between K_1 and microsphere flow was observed when all three factors were corrected as described in Eq. 1 (Fig. 6e). Results of the regression analysis also demonstrated the highest correlation coefficient when all three correction factors were applied. Table 1 summarises the results of the Akaike information criteria (AIC) and Schwartz criteria (SC) obtained from the kinetic fitting analysis for all myocardial segments of all subjects. Both

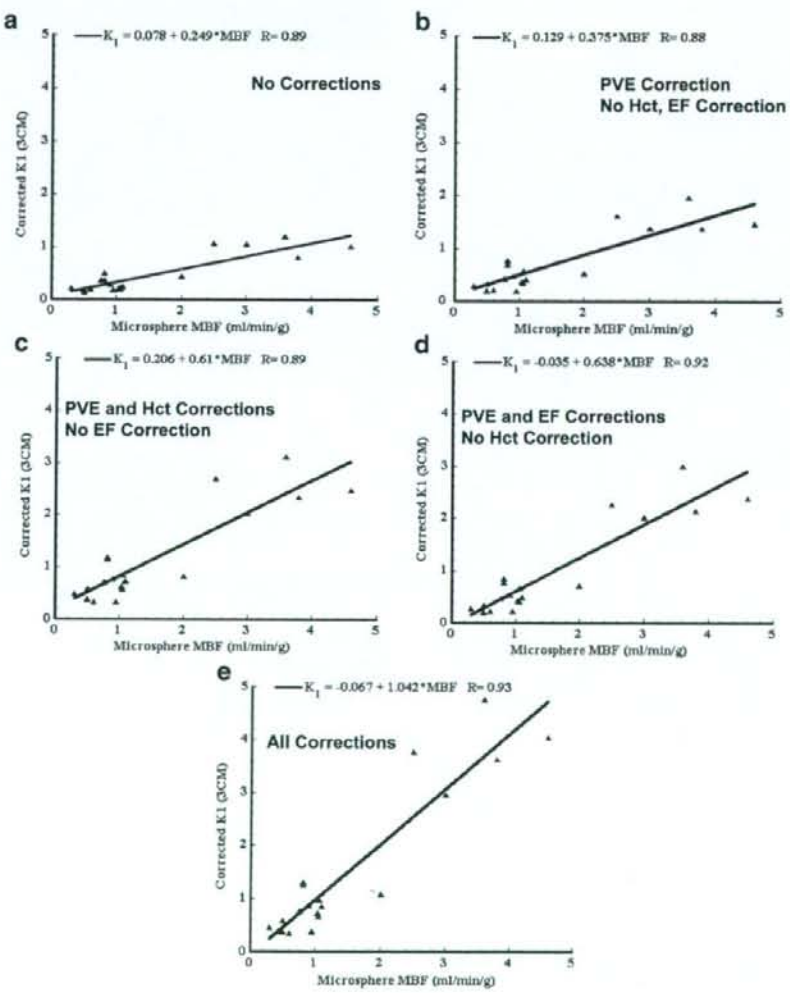

Fig. 6 Plot of K_1 derived from the three-compartment model fit against the mean of the pre- and post-dynamic SPECT microsphere blood flow measurements. **a** No correction for PVE, limited first-pass EF or conversion from plasma to blood flow has been applied. **b** Correction for PVE has been applied, but not for Hct or limited first-pass EF. **c** Corrections for PVE and Hct have been applied, but not for limited first-pass EF. **d** Corrections for PVE and limited first-pass EF have been applied, but not for Hct. **e** All corrections are applied for PVE, limited first-pass EF and Hct

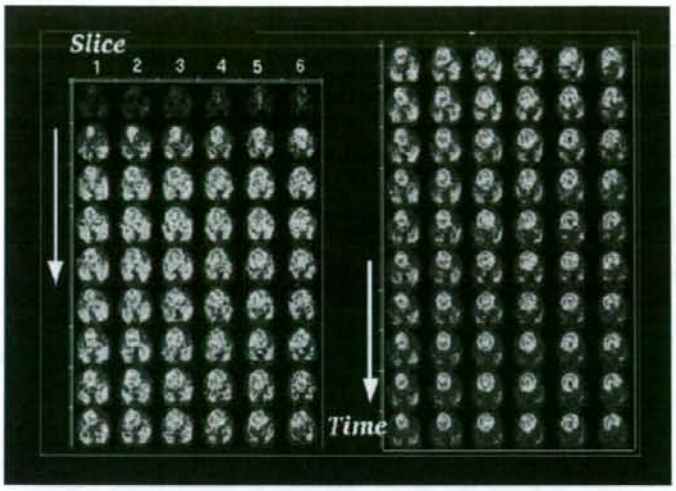

Fig. 4 A typical example of sequential SPECT images of the myocardium for six representative slices after intravenous injection of ^{201}Tl into a canine at rest

Fig. 3. The plasma to whole blood ratio curves could be approximated by the following equation:

$$R_{pl/wb} = A_0 e^{-\lambda(t+\Delta t)^2} + A_1\left(1 - e^{-\lambda_2(t+\Delta t)}\right), \quad (3)$$

which resulted in A_0=1.303±0.045, A_1=0.7649±0.0056, λ_1=0.03636±0.0039 min^{-1}, λ_2=0.1263±0.0077 min^{-1} and Δt=0.9516±0.41 min. The correlation coefficient for the fit was r=0.995.

Figure 4 shows a typical example of sequential images after the intravenous injection of ^{201}Tl for six representative slices of a dog studied at rest. It can be seen that ^{201}Tl appeared in the ventricular chambers first and then gradually accumulated homogeneously into the left myocardium. The quality of these images is reasonably good, indicating that our approach of estimating the kinetic parameters by NLLSF is feasible without excessive noise

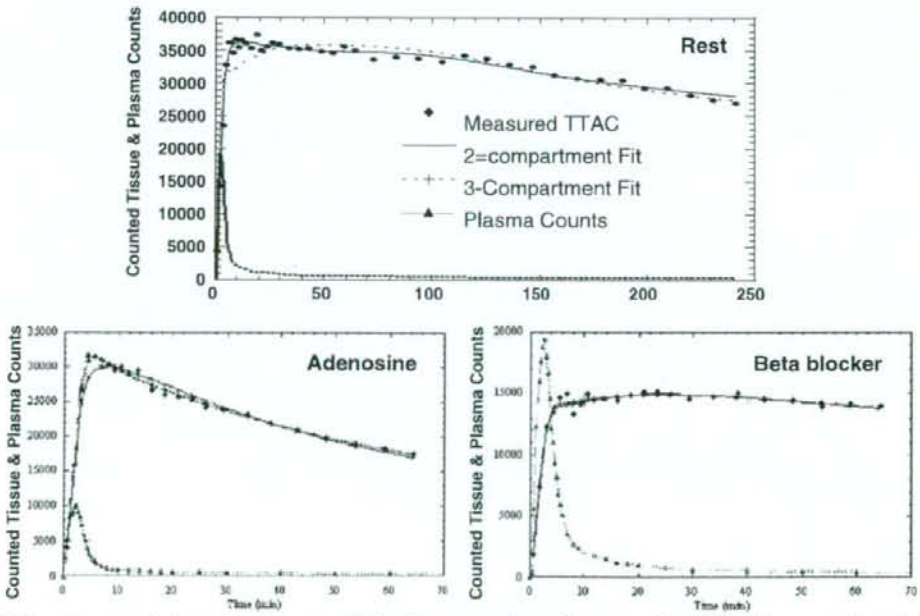

Fig. 5 TTACs and two- and three-compartment model fits for a resting, adenosine (increased MBF) and beta-blocker (reduced MBF) study. Note the different time scales for the resting study because resting studies were collected for 4 h compared to ≈1 h for the pharmacological intervention studies

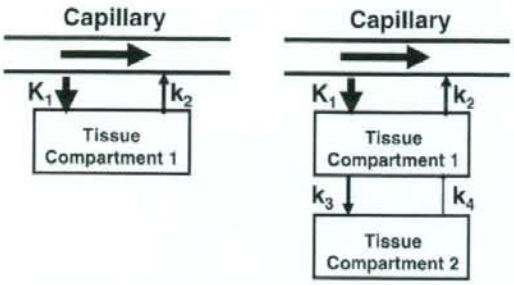

Fig. 2 Two- and three-compartment models evaluated in this study. K_1 in units of ml/min/g denotes the regional MBF for both models. Distribution volume (V_d) in units of ml/g is defined as K_1/k_2 for the two-compartment mode, and $\frac{K_1}{k_2}\left(1+\frac{k_3}{k_4}\right)$ for the three-compartment model

The physiological basis for the correction factors in Eq. 1 can be described as follows:

1. TTACs obtained from SPECT images are under-estimated due to the limited spatial resolution relative to the myocardial wall thickness and also due the myocardial contractile motion. This phenomenon is known as PVE. The PVE correction factor for each TTAC was determined from the ratio of the last SPECT frame counts to the ^{201}Tl myocardial tissue sample counts obtained from the tissue samples taken and measured with the well counter at the end of the SPECT scan.
2. The arterial input function for the compartment model studies was defined from the plasma radioactivity concentration curve, rather than the whole blood radioactivity curve. K_1 is therefore the regional "plasma" flow. Thus, for comparison with the microsphere flow measurements, which estimates the whole blood flow, K_1 was divided by (1−Hct) to obtain the flow for the total blood.
3. For a tracer with limited first-pass EF<1.0, flow (MBF) is related to K_1 by K_1=EF×MBF. The first-pass EF is flow-dependent and decreases at high flow. We have applied an empirical formulation for the first-pass EF based on the data by Weich et al. [10] ($EF=0.84-0.524\cdot\log_{10}(K_1^*)$ where K_1^* is $K_1/(1-Hct)$. The K_1 values obtained with two- and three-compartment models with/without corrections according to Eq. 1 were compared to the average of microsphere blood flow values obtained pre- and post-dynamic SPECT scan.

The distribution volume of ^{201}Tl (V_d) was defined as

$$V_d = \frac{K_1}{k_2} \text{ for the two} - \text{compartment model} \quad (2a)$$

$$V_d = \frac{K_1}{K_2}\left(1+\frac{K_3}{K_4}\right) \text{ for the three} - \text{compartment model.} \quad (2b)$$

As mentioned before, the resting studies were collected for 4 h, whilst the adenosine and beta-blocker studies were collected for approximately 1 h. To investigate whether the shorter collection time introduces systematic bias, NLLSF fits restricted to the first 1 h of the resting study data were also performed and compared with the V_d values from the full 4 h resting data set and with the estimates obtained from the beta-blocker and adenosine studies.

Akaike information criterion (AIC) and Schwarz criterion (SC) were calculated for both two-compartment and three-compartment model fits [16] to test the adequacy of the two models. All data are presented as mean±1 SD. Student's t test was employed in the comparison of the V_d values. Pearson's regression analysis was applied to compare K_1 and microsphere flow values. A probability value of <0.05 was considered statistically significant.

Results

Figure 3 shows the plasma to whole blood concentration ratios in the six dogs with rapid plasma separation and the averaged data. Equilibrium is reached after about 40 min, at which time the mean ratio was found to be 0.76. As expected, relative plasma concentration is highest early on as the tracer is injected into the plasma (and not red blood cells). ^{201}Tl is rapidly cleared from the plasma causing a rapid decline in relative plasma concentration and "undershoot" before equilibrium is established. Samples left for a prolonged period before plasma separation showed the value of approximately 0.78, which was close to the plasma to whole blood concentrations ratio at the equilibrium shown in

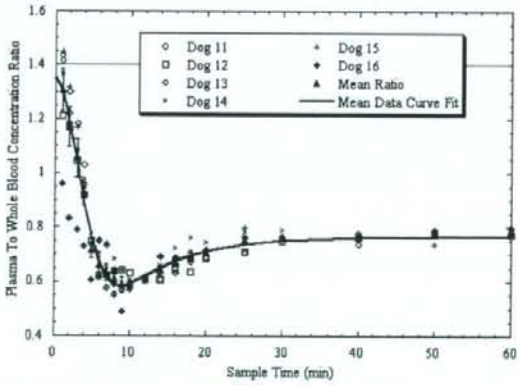

Fig. 3 Individual and mean plasma to whole blood concentration ratios over time for the six dogs with rapid plasma separation. *Error bars* indicate the standard error of the mean. *Solid line* is the curve fit to mean ratio data

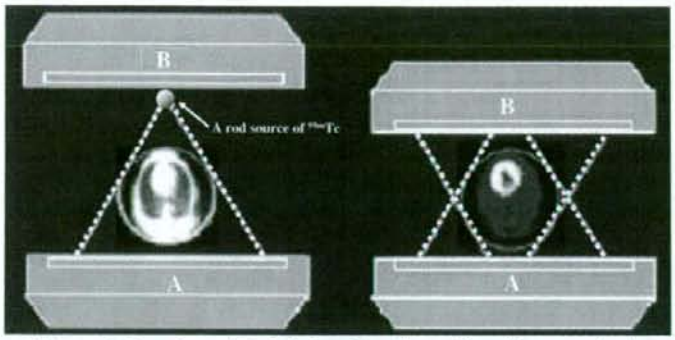

Fig. 1 Schematic diagram of data acquisition using a clinical dual-headed SPECT camera fitted with fan-beam collimators. Transmission scan was performed using a ^{99m}Tc-filled rod source placed at a focal line of one of the collimators, and only one of the detectors was used (*left*). Both detectors were used in the emission scan (*right*)

window centred on 77 keV was used for the ^{201}Tl acquisitions [4, 13].

Arterial blood samples were taken every 20 s for the first 6 min, every 60 s for 6–10 min, 120 s for 10–20 min, 300 s for 20–30 min and 600 s for 30–60 min. For the resting studies, blood samples were also taken every 20 min for 1–2 h and additional samples at 2.5, 3 and 4 h post-^{201}Tl infusion. In six studies, plasma was separated immediately after sampling by centrifugation, and plasma samples were counted in a well counter cross-calibrated with the SPECT scanner. To minimise the effects of the continued exchange of ^{201}Tl between plasma and red blood cells in the test tubes after sampling, immediate, rapid separation of plasma from whole blood was required. An averaged relationship between plasma and whole blood concentration ratio over time was obtained, and then multiplied with the whole blood curves for all studies to derive a plasma input function.

At the end of the SPECT study, the microsphere blood flow measurement was repeated with ^{51}Cr microspheres. The dogs were then killed by injection of potassium chloride (KCl) and the myocardium was dissected into samples suitable for counting in the well counter. The ^{201}Tl concentration in the tissue samples was derived from the sample weight normalised gamma counter counts. The samples were stored to allow for the decay of ^{201}Tl ($T_{1/2}$= 73 h vs $T_{1/2}$=32.5 days for ^{141}Ce and 27.8 days for ^{51}Cr) and then counted to measure the ^{141}Ce and ^{51}Cr activities. Separation between ^{141}Ce and ^{51}Cr counts was based on their respective gamma ray energies (145 keV for ^{141}Ce and 323 keV for ^{51}Cr).

SPECT data processing

Projection data were processed according to previously described procedures [5]. Briefly, the transmission data obtained by the fan-beam collimator were first re-binned into parallel projections. Transmission projections were normalised by blank projection, re-constructed to generate quantitative maps of the attenuation coefficient for ^{99m}Tc and then linearly scaled to provide attenuation correction maps for ^{201}Tl. Emission data were corrected for detector non-uniformity and also re-binned into parallel projections. The projection data were then corrected for scatter with transmission-dependent convolution subtraction (TDCS) originally proposed by Meikle et al. [14] and further optimised by our group [4, 5]. The emission projection data were re-constructed with the OS-EM reconstruction algorithm [15] using three iterations and ten subsets. The re-constructed images were cross-calibrated with the well counter system.

Data analysis

Re-constructed images were normalised by acquisition time for each frame. Multiple circular regions of interest (ROI) were drawn on the myocardium, and the TTAC of ^{201}Tl were generated for the anterior, apical, lateral, posterior and septal areas of the myocardium. The two-compartment model (one tissue compartment) and three-compartment model (two tissue compartments) shown in Fig. 2 were applied to determine two parameters (K_1 and K_2) for the two-compartment model and four parameters (K_1–K_4) for the three-compartment model by means of non-linear least squares fitting (NLLSF).

The regional MBF was considered to be related to K_1 obtained from compartment model fits. K_1 is, however, affected by the PVE, Hct and the limited first-pass EF whose effects were corrected according to Eq. 1:

$$\mathrm{MBF} = \frac{\mathrm{PVE}}{\mathrm{EF} \times (1 - \mathrm{Hct})} \times K_1 \qquad (1)$$

exercise-induced myocardial ischaemia and/or for assessing myocardial viability in patients with coronary artery disease. The diagnosis, however, has been limited to qualitative or visual assessment of the physical extent of the defect areas rather than quantitative assessment of physiological functions. Quantitative methods would for example enable longitudinal studies when assessing therapy response and pharmacological interventions. Some groups have already investigated the feasibility of estimating quantitative parameters with dynamic SPECT in the myocardium using ^{201}Tl [1] and ^{99m}Tc-Teboroxime [1, 2], but these techniques have not yet been applied to clinical practice. This is largely attributed to the fact that quantitative reconstruction programmes are not readily available on commercial SPECT systems.

We have developed a reconstruction programme package for SPECT, which can accurately provide quantitative images of radio-labelled tracer distributions in vivo, which is a pre-requisite for absolute physiological parameter estimation. The adequacy and accuracy of these methods have been demonstrated in multiple papers for ^{99m}Tc and ^{201}Tl in cardiac studies [3–5], and for ^{99m}Tc and ^{123}I in brain studies [6]. It has also been demonstrated, in brain studies, that physiological parameters such as cerebral perfusion [6] and cerebral flow reactivity [7] obtained using our package were as accurate as those determined by PET. These findings suggest that absolute quantitation of regional myocardial perfusion might also be possible in a clinical setting using commercial SPECT cameras.

^{201}Tl is a potassium analogue, and its kinetics has been extensively investigated in previous studies [8, 9]. Due to the high first-pass extraction fraction (EF) [10] and a large distribution volume, ^{201}Tl has been considered an ideal tracer for quantitation of absolute myocardial blood flow, not only at rest but also at hyperemic conditions. As a clinical implication, quantitative assessment of MBF and coronary flow reserve is important. For instance, coronary microvascular dysfunction or impaired endothelial function in patients with coronary risk factors or patients with cardiomyopathy or with heart failure is an un-resolved important issue to answer [11]. Coronary flow reserve can also be reduced in patients with hyper-cholesterolemia without overt coronary stenosis [12]. The low energy and long half-life of ^{201}Tl have, however, seriously limited its use in nuclear cardiology.

The goal of this study was to validate our reconstruction methodology for the estimation of myocardial blood flow using ^{201}Tl and dynamic SPECT using tissue time–activity curves (TTAC) derived from myocardial regions. In addition, we aimed to find the optimal kinetic model configuration and to investigate the factors affecting the estimation of physiological parameters such as the partial volume effect (PVE), appropriate choice of input function, conversion from plasma to blood flow using haematocrit (Hct) and the limited first-pass tracer EF.

Materials and methods

Subjects

A total of 21 dogs were studied in which 8 were in a resting condition, 9 dogs during constant infusion of adenosine for increased MBF, and 4 dogs during constant infusion of beta-blocker. Of the 21 studies, 1 study was un-successful and projection data could not be retrieved from the scanner, reducing the number of resting studies to 7 and total dog studies to 20. Adenosine was infused continuously over the study duration at a rate ranging from 140 to 700 mg/kg/h to achieve a range of blood flow increases. An initial dose of beta-blockers ranging from 2 to 6 mg was given, followed by a constant infusion for the duration of the study of 2 or 4 mg/h. The study protocol was approved by the animal ethics committee at the Akita Research Institute of Brain, Akita City, Japan where all experiments were carried out.

SPECT procedures

All dogs were anaesthetised, and the catheters for dose administration and arterial blood sampling were inserted before the study. The SPECT system was a conventional dual-head gamma camera (Toshiba GCA-7200A, Tokyo, Japan) fitted with short focal length fan-beam collimators (LEHR-Fan). The transverse field-of-view (FOV) was 22 cm diameter and axial FOV was 20 cm. The dogs were carefully taped into a cradle to minimise motion during the study, and also to ensure that no truncation occurred. Heart rate and blood pressure were monitored throughout the study and recorded at regular intervals.

Before the injection of any tracer, a 15-min transmission study was carried out in which a rod source filled with approximately 740 MBq of ^{99m}Tc was placed along the focal line of one of the fan-beam collimators (see Fig. 1). The transmission study was followed by injection of 3 MBq of ^{141}Ce microspheres into the left ventricle via a catheter and blood was withdrawn from the aorta at a constant flow rate of 5 ml/min for 2 min to serve as an input function. For the pharmacological intervention studies, adenosine infusion or beta-blocker injection followed by infusion was commenced before the ^{141}Ce microsphere administration.

Dynamic SPECT was commenced with the start of the 4-min constant infusion of 110 MBq ^{201}Tl. The frame collection rates and 360° rotation times were 10×1 min (rotation time 15 s), 6×2 min (30 s), 3×4 min (60 s) and 5×5 min (60 s) for the first hour for all studies. Resting blood flow studies had an additional 18×10 min (120 s) frames collected for a total study period over 4 h. The shorter total study time for the drug infusion studies was mandated by the difficulties in keeping the dogs stable with prolonged infusions of the drugs used. A 34% energy

Eur J Nucl Med Mol Imaging
DOI 10.1007/s00259-007-0654-4

ORIGINAL ARTICLE

Absolute quantitation of myocardial blood flow with ^{201}Tl and dynamic SPECT in canine: optimisation and validation of kinetic modelling

Hidehiro Iida · Stefan Eberl · Kyeong-Min Kim · Yoshikazu Tamura · Yukihiko Ono · Mayumi Nakazawa · Antti Sohlberg · Tsutomu Zeniya · Takuya Hayashi · Hiroshi Watabe

Received: 18 September 2007 / Accepted: 4 November 2007

Abstract
Purpose ^{201}Tl has been extensively used for myocardial perfusion and viability assessment. Unlike ^{99m}Tc-labelled agents, such as ^{99m}Tc-sestamibi and ^{99m}Tc-tetrofosmine, the regional concentration of ^{201}Tl varies with time. This study is intended to validate a kinetic modelling approach for in vivo quantitative estimation of regional myocardial blood flow (MBF) and volume of distribution of ^{201}Tl using dynamic SPECT.
Methods Dynamic SPECT was carried out on 20 normal canines after the intravenous administration of ^{201}Tl using a commercial SPECT system. Seven animals were studied at rest, nine during adenosine infusion, and four after beta-blocker administration. Quantitative images were reconstructed with a previously validated technique, employing OS-EM with attenuation-correction, and transmission-dependent convolution subtraction scatter correction. Measured regional time–activity curves in myocardial segments were fitted to two- and three-compartment models. Regional MBF was defined as the influx rate constant (K_1) with corrections for the partial volume effect, haematocrit and limited first-pass extraction fraction, and was compared with that determined from radio-labelled microspheres experiments.
Results Regional time–activity curves responded well to pharmacological stress. Quantitative MBF values were higher with adenosine and decreased after beta-blocker compared to a resting condition. MBFs obtained with SPECT (MBF_{SPECT}) correlated well with the MBF values obtained by the radio-labelled microspheres (MBF_{MS}) ($MBF_{SPECT}=-0.067+1.042\times MBF_{MS}$, $p<0.001$). The three-compartment model provided better fit than the two-compartment model, but the difference in MBF values between the two methods was small and could be accounted for with a simple linear regression.
Conclusion Absolute quantitation of regional MBF, for a wide physiological flow range, appears to be feasible using ^{201}Tl and dynamic SPECT.

Keywords Myocardial blood flow · Dynamic SPECT · Thallium-201 · Compartment model · Quantitation

H. Iida (✉) · S. Eberl · K.-M. Kim · M. Nakazawa · A. Sohlberg · T. Zeniya · T. Hayashi · H. Watabe
Department of Investigative Radiology,
National Cardiovascular Center Research Institute,
Fujishiro-dai,
Suita City, Osaka 565-8565, Japan
e-mail: iida@ri.ncvc.go.jp

S. Eberl
PET and Nuclear Medicine Department,
Royal Prince Alfred Hospital,
Missenden Road,
Camperdown, NSW 2050, Australia

Y. Tamura
Department of Cardiology, Akita Kumiai General Hospital,
1-1-1, Nishi-bukuro, Iijima,
Akita City 011-0948, Japan

Y. Ono
Akita Research Institute of Brain,
6-10, Senshu-Kubota Machi,
Akita City 010-0874, Japan

Introduction

Myocardial perfusion imaging using Thallium-201 (^{201}Tl) is well established in routine clinical practice for detecting

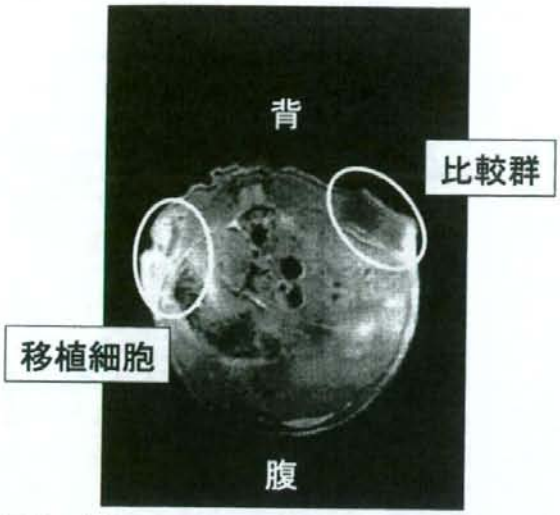

図 13　高分子化ＭＲＩ造影剤を封入した細胞を皮下に移植したマウスの MRI 断層写真

日間にわたって、細胞からの造影剤の有意な漏出は認められなかった。このことより、1 年程度は、移植細胞を MRI により追跡できる性能を有していると考えられる。図 13 は、標識した NIH3T3 細胞を皮下に埋入したマウスの、MRI 断層写真である。移植細胞がはっきりと確認できる。細胞内に存在する極微量の水を介して撮像可能なコントラストが得られていることは、キャリアーとして選択した PVA 分子が Gd 周囲環境の水を確保しているためかも知れない。本造影剤により、大動物を用いた前臨床研究における細胞移植療法治療効果のメカニズム解明が可能になるのみでなく、移植細胞数を最低限に抑えることにより、最低限のリスクで、最大の治療効果を発揮させるための定量的指標を得られるであろう。

Ⅵ. さいごに

再生医療の研究が進むとともに、得られた有用細胞を組織や臓器へと 3 次元構築する困難さ、あるいは、もっとも単純と思われる自己細胞移植でさえ、あらゆる問題が浮上している。ますます加速する幹細胞研究に後れを取らないように、工学技術の開発研究を進めなくてはならない。

● 参考文献

1) “再生医工学”、筏義人編、化学同人 (2001)
2) R. Langer and J. P. Vacanti, Science, 260, 920-926 (1993)
3) J. A. Thomson, J. Itskovitz-Eldor, S. S. Shapiro, M. A. Waknitz, J. J. Swiergiel, V. S. Marshall, J. M. Jones, Science, 282, 1145(1998)
4) Y. Miyahara, N. Nagaya, M. Kataoka, B. Yanagawa, K. Tanaka, H. Hao, K. Ishino, H. Ishida, T. Shimizu, K. Kangawa, S. Sano, T. Okano, S. Kitamura, H. Mori, Nat. Med., 12(4), 459(2006)
5) S. W. Kim, H. Han, G. T. Chae, S. H. Lee, S. Bo, J. H. Yoon, Y. S. Lee, K. S. Lee, H. K. Park, K. S. Kang, Stem Cell, 24, 1620(2006)
6) J. Mauduit, E. Perous, M. Vert, J Biomed Mater Res, 30, 201-207(1996)
7) Y. Ikada, Y. Shikinami, Y. Hara, M. Tagawa, E. Fukada, J Biomed Mater Res, 30:553-558(1996).
8) R. E. Johnson, J. A. Lanaski, V. Gupta, M. J. Griffen, H. T. Gaud, T. E. Needham, H. Zia, J Controlled Release, 17:61-67(1991).
9) N. Nihant, C. Schugens, C. Grandfils, R. Jerome, R. Teyssie, Pharm Res, 11:1479-1484(1994).
10) A. Echeverria J. Jimenez, Surgery, 131, 1-13 (1970).
11) Y. Kimura, K. Shirotani, H. Yamane, T. Kitao, Polymer, 34(8):1741-1748(1993).
12) T. Yamaoka, Y. Hotta, K. Kobayashi, and Y. Kimura, Synthesis and properties of malic acid-containing functional polymers, Int. J. Biol. Macromol., 25(1-3), 265-271(1999)
13) 山岡哲二、竹部義之、木村良晴：高分子論文集、1998, 55、328-333
14) T. Yamaoka, Y. Takahashi, T. Ohta, M. Miyamoto, A. Murakami, and Y. Kimura, J. Polym. Sci. Part A: Polym. Chem., 37, 1513-1521(1999)
15) T. Yamaoka, Y. Takahashi, T. Fujisato, C. W. Lee, T. Tsuji, T. Ohta, A. Murakami, and Y. Kimura, J. Biomed. Mater. Res., 54(4), 470-479(2001)
16) T. Fujiwara, T. Mukose, T. Yamaoka, H. Yamane, S. Sakurai, and Y. Kimura, Macromol. Biosci., 1, 204-208(2001)
17) Tachibana Y, Ennmi J, Iida H, Yamaoka T, Abstract for SFB 2007 Annual meeting, 94(2007)

成などを調節して37℃でゲル化することに成功したインジェクタブルスキャホールドの写真を図10に示した。X線散乱測定により、温度上昇とともにステレオコンプレックス結晶が成長することがそのメカニズムであることも証明された。得られたゲルの含水率は90%以上であり、その物質透過性に優れること、さらに、細胞毒性を誘発する一切の化学物質を利用していないために、細胞生存率を下げることなく、対象部位に細胞を注入できる材料となる。図11は、このことを示す *in vitro* 実験の結果である。混合ミセル液にGFP(緑色蛍光タンパク)組換マウス胎児線維芽細胞を懸濁させて、アガロースゲル中で昇温ゲル化させた3日後にも、細胞は正常な携帯とGFP発現機能を維持する。

VI. 細胞トラッキング

細胞移植療法のもう一つの大きな課題は、その治療メカニズムが未だ不明なことである。すなわち、組織再生や機能改善が、移植した細胞自身の増殖により機能が回復したためによるのか、あるいは、移植した細胞が産生する生理活性物質などに対してレシピエント(移植を受けた患者)が反応することで治癒したパラクライン効果によるものかを解明する手だてがない。特に、自家細胞移植では免疫染色で移植した細胞を区別することさえも困難である。一つの手法として、GFP(+)の細胞をGFP(-)マウスに移植して *in vivo* 蛍光イメージング装置で追跡する手法があるが、蛍光の特性により、ラット程度の小動物が限界である。最近、我々は、移植した細胞をMRIで低浸襲的に追跡するための、新たな細胞標識用MRI造影剤の開発に成功した。この目的を達成するには、磁性を有する分子(ガドリニウム錯体など)を移植細胞の細胞質内に長期間安定に滞留させる技術が必須となる。さらに、細胞の増殖や機能発現を妨げることなく、細胞が死滅したときには、この造影剤が速やかに体外へ排泄されることが必要である。図12に、本システムの概要を示した。ガドリニウム錯体分子(丸印)の細胞膜透過性を抑制し、かつ、細胞に対する毒性を軽減させるために高分子キャリアーを用いた。この高分子化造影剤は、微弱な電気的ショックを細胞に加える手法により、あらゆる細胞に対して容易に送達することができる[17]。NIH3T3細胞、および、ラット間葉系幹細胞を、本造影剤にて標識したところ、その細胞増殖性は、10

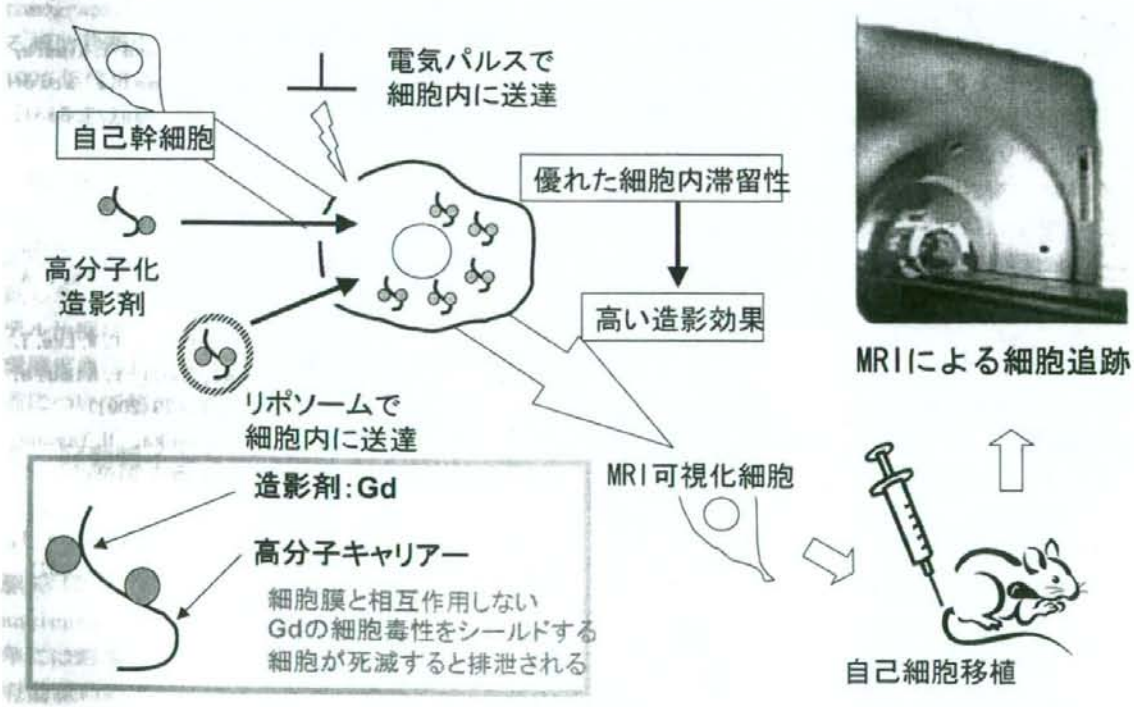

図12　移植した自己幹細胞をＭＲＩにより追跡するための高分子化ＭＲＩ造影剤システム

植術であるが、まだまだ、問題も多い。例えば、細胞懸濁液を直接組織などに注入した場合には、細胞を効率よく患部に留められない。そこで、細胞注入を支援する材料として、体内で、水溶液から含水ゲルへ変化する生体吸収性材料（インジェクタブルスキャホールド）が注目されている。従来から、光反応性基や、化学反応性基、あるいは、ポリ（N-イソプロピルアクリルアミド）などの温度応答性ポリマーが利用されたが、いずれも、その生体内での安全性は確保されていない。我々は、PLA とポリエチレングリコール（PEG）という、生体内での利用実績に優れる２つの高分子材料のみを利用することで、温度応答性を実現させインジェクタブルスキャホールドとすることに成功した。

京都工芸繊維大学木村良晴教授らとの共同研究の中で、いろいろなミセルを AFM で観察していた時、ある条件を満たしたミセルが、加熱処理によってナノ繊維構造に変化することを、偶然、見いだした[16]。ミセルからナノ繊維への変化には、隣接するミセル同士が相互作用（コアを形成するポリ乳酸部分が、コロナ構造を形成する PEG 層を乗り越えて融合）する必要がある。そこで、ポリ -L- 乳酸からなるミセル（L 体ミセル）と、ポリ -D- 乳酸からなるミセル（D 体ミセル）の分散液を混合することを発案した（**図９左**）。というのも、加熱により隣接する L 体ミセルと D 体ミセルが融合すると、ステレオコンプレックスミセルが形成し、その結果、**図９右**に示すように３次元架橋構造が成長してゲル化するというアイデアである。ポリ乳酸のステレオコンプレックスは、ホモ結晶に比べて融点が約 50℃も高い安定な構造であることも、ゲル化を促進して安定化することに寄与すると考えられる。実際に、共重合

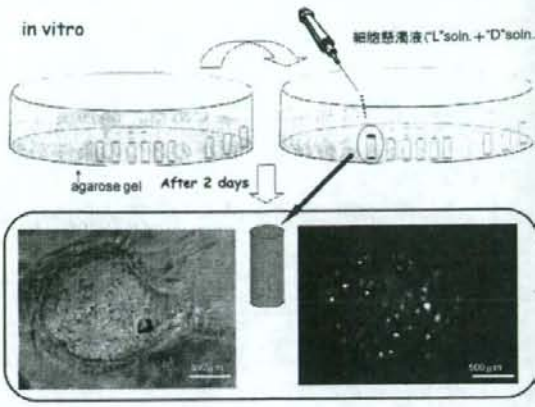

図 11　L 体ミセル・D 体ミセル混合液に対して、GFP 遺伝子組み換え細胞を混合し、in vitro でゲル化させることで、このゲル内での細胞生存性が確認された。

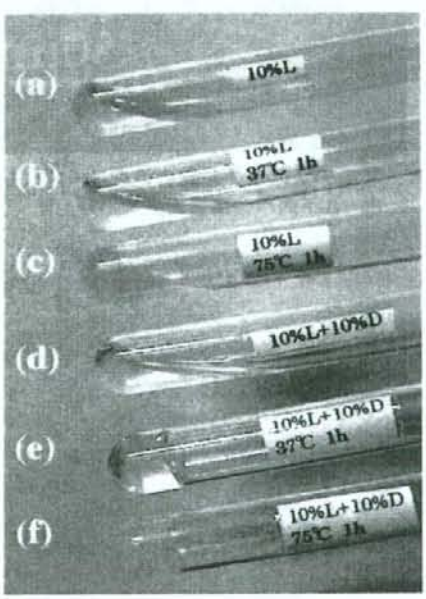

The aqueous dispersion (10wt%) of PLLA-PEG-PLLA (1300-4600-1300)
(a) r.t.
(b) 37°C for 1 h
(c) 75°C for 1 h
The mixture of each dispersion (10wt%) of PLLA-PEG-PLLA (1300-4600-1300) and PDLA-PEG-PDLA (1100-4600-1100)
(d) r.t.
(e) 37°C for 1 h
(f) 75°C for 1 h

図 10　L 体ミセルと D 体ミセル混合液（d）は、37 度に加温することで透明なゲルに転移する（e）。それに対して、L 体ミセルのみの分散液 (a) は 75 度で白濁はするがゲル化には至らない。

めに、周囲から積極的に細胞が浸潤して組織と置換される。それに対して、PLAなどでは、非酵素的加水分解の結果生成した間隙で細胞が増殖する。我々は、ポリ乳酸と水溶性ポリエーテル(PEth)とのブロック共重合体を開発し、高親水性かつコラーゲンゲルの様な軟組織再生を誘導する合成スキャホールドとして利用することを目的に開発を進めた[14]。一般的には、従来のPLA/PEthブロック共重合体は、図7に示したPEth末端の水酸基を開始点とするラクチドの開環重合により合成されるトリブロック共重合体である。このトリブロック共重合体は、薬物担体などとしては有用であるが、強度が要求されるスキャホールドには利用が困難である。高強度で高含水率を有する共重合体には以下の3つの条件が要求される。

- 十分な力学的強度を得るためには、100,000程度の分子量が必要。
- PEthの分子量が、腎臓から排泄される20,000程度以下であることが必要。
- 十分な含水性を達成するためには、数十%以上のPEth組成が必要。

これら3つの条件を満たす共重合体は、トリブロック体では合成が不可能であり、(AB)n型マルチブロック共重合体が必須である。そこで、オリゴ乳酸とPEthの直接縮合反応によりマルチブロック共重合体を開発した(図7)。所定量のデカンジカルボン酸を系中の水酸基とカルボキシル基を等モル量に調節するために添加し、さらに、ジフェニルエーテルを溶媒とした環流により脱水重縮合を加速させる。PEth組成の上昇と共に共重合体の分子量が低下するトリブロック共重合体とは異なり、マルチブロック共重合体では、PEth組成に関係なく分子量100,000以上を実現することに成功した。その結果、速い分解速度と親水性表面を有しながらも十分な初期破断強度を有する繊維、メッシュ、フィルム、不織布、スポンジなどを調製することが可能となった。このマルチブロック共重合体は、PEth組成の上昇とともに、含水率が上昇し、ラット皮下に埋入実験において、ほとんどカプセル化も認められず、炎症反応も軽微であった[15]。これらの含水性マルチブロック共重合体をベースにして作製した、組織誘導性スキャホールドによる皮膚組織再生においては、スキャホールド内での毛細血管網構築性が確認されている(図8)。

V. 細胞移植を支援するインジェクタブルスキャホールド

上述の如く、臨床化が大いに期待される幹細胞移

図8 マルチブロック共重合体をベースにしたスキャホールド内への血管新生

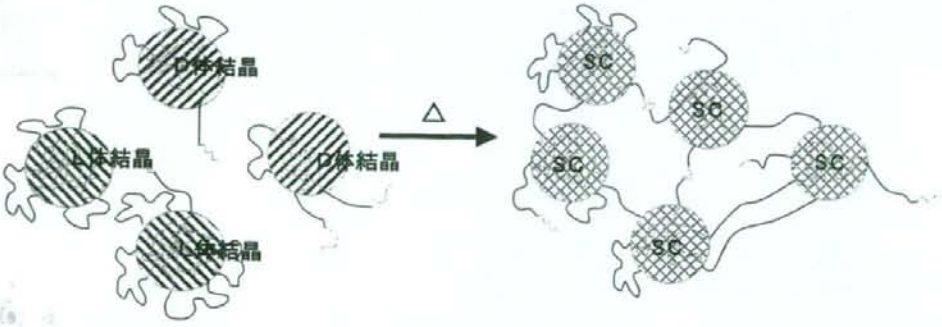

図9 L体ミセル/D体ミセル混合溶液の温度応答性ゲル化メカニズム

の表面を、所定濃度の NaOH で加水分解することで表面にカルボキシル基を導入し、カルボジイミド法により、抗 CD34 抗体を固定化した。この抗体修飾スキャホールド上に、CD34 陽性のモデル細胞（KG-1a 細胞）、CD34 陰性のモデル細胞（HL60）、および、イヌ骨髄細胞を約 2×10^6 個 /50ml の濃度で、流速 0.05ml/min で播種し、接着した細胞数を WST-1 法により計数し、接着細胞種は、免疫染色にて評価した。抗体固定化スキャホールド上には、オリジナルスキャホールドに対して、約 4 倍の CD34 陽性細胞が吸着し、さらに、KG-1a 細胞と HL60 細胞の混合モデル細胞系では、80% 程度の CD34 陽性細胞濃縮効率が得られ、また、イヌ骨髄細胞播種システムに於いても、有意な CD34 陽性細胞の選択播種が確認された。現在、その効率を向上させるべく、抗体固定化濃度の向上と配向化を進めている。

Ⅳ. ポリ乳酸系含水ゲルの開発

PGA や PLA の多孔質体では疎水性が高いために水分を多く含む軟組織との親和性には問題がある。図 6 には、ポリ乳酸不織布を用いた場合と、コラーゲンゲルを用いた場合の組織再生の違いについて示した。コラーゲンゲルは、軟組織との親和性が高いた

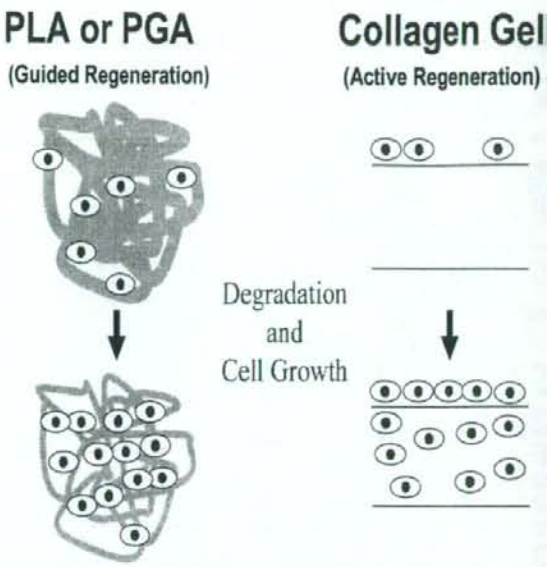

図 6　PLA などの疎水性の生体吸収性材料とコラーゲンゲルとではその組織再生機構が大きく異なる

Synthesis of Triblock Copolymers

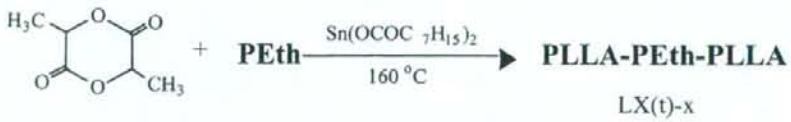

Synthesis of Multiblock Copolymers

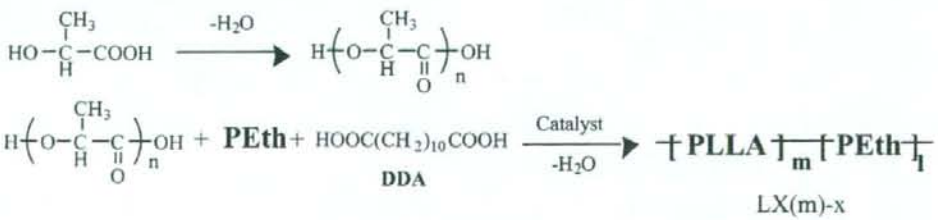

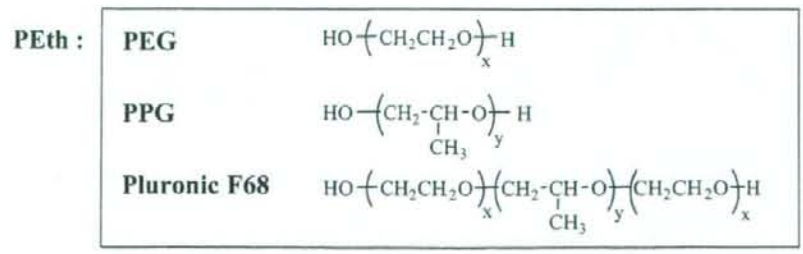

図 7　ポリ乳酸とポリエーテルからなるトリブロック、および、マルチブロック共重合体の合成方法

なランダム共重合体の分解速度を示した[10]。分解はアモルファス領域から進むので、少量の他成分モノマーとの共重合により結晶化度が低下して分解速度が飛躍的に上昇する。一方、官能基を側鎖に有する環状モノマーとの開環共重合により、側鎖に官能基を有するPGA誘導体やPLA誘導体が得られる。生体内に埋入されるPLA系材料には、高い組織親和性や細胞親和性などの生物学的表面特性が要求されることも多いが、側鎖に官能基をもたないPLAの表面修飾は容易ではない。そこで、官能基を有する生体吸収性PLA誘導体が精力的に研究された[11]。導入された官能基に対して、細胞特異的接着リガンドを固定化することで、固定化量に依存した優れた細胞親和性が達成できている[12]。

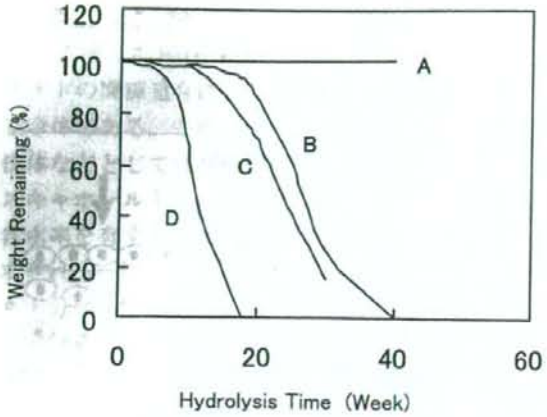

図4　ポリ乳酸誘導体の分解速度
(A) PLA, (B) PLA-co-ポリεカプロラクトン(50:50), (C) PLA-co-ポリεカプロラクトン(75:25), および (D) ポリグリコール酸

このようなモノマー合成を伴うランダム共重合法は、特別な合成施設と技術が要求されるため、さらに簡便な手法として、ラジカル反応法や表面加水分解法の開発が重要である[13]。一方、造血幹細胞やEPCを用いた血管再生が期待され、モノクローナル抗体を用いた磁気ビーズ法や、蛍光剤を用いたFACS法により単離した細胞の利用が試みられているが、操作が困難であり、必ずしも臨床に適した方法ではない。そこで、造血幹細胞を選択的に吸着する生体吸収性スキャホールドに対して、採取した骨髄細胞を直接播種して移植できる治療システムの構築を目指した（図5）。すでに血管再生用スキャホールドとして用いられているポリ乳酸の多孔質体

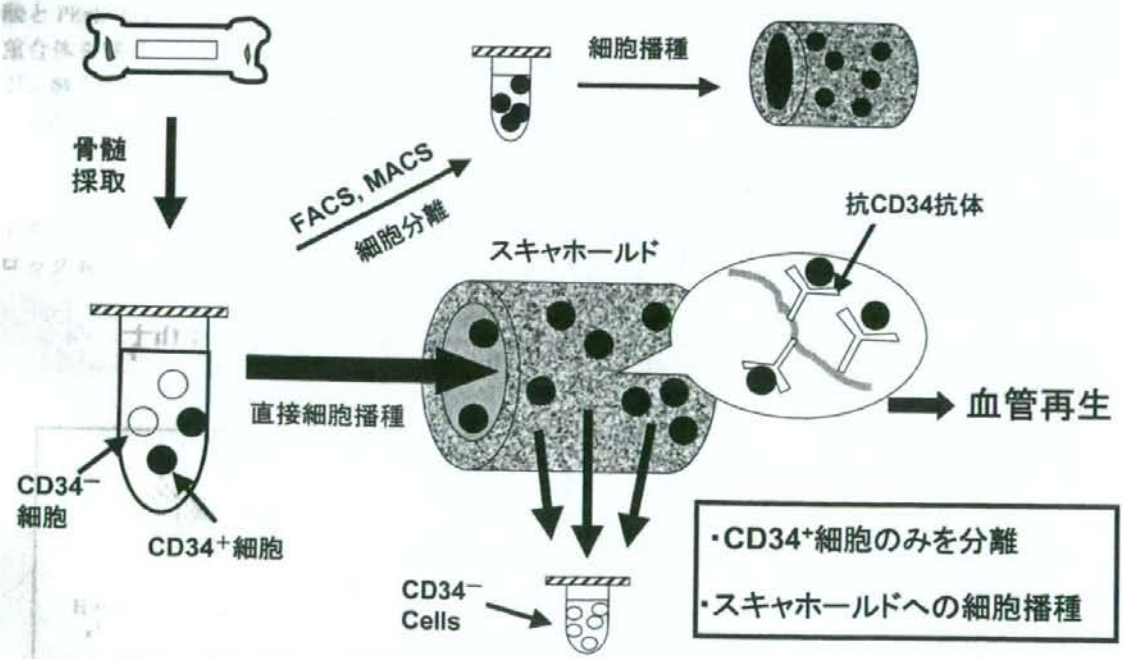

図5　幹細胞特異的抗体を表面に固定化した血管再建用スキャホールドは、骨髄細胞中のCD34陽性細胞のみをトラップする

上述の例では、スキャホールドとして、PGA不織布やコラーゲン多孔質体が使われた。これに対して、より古くから研究されていた**図1の①**は、スキャホールドのみを使って、*in vivo* で、組織再生を試みる戦略であり、組織再生誘導法（GTR, Guided Tissue Regeneration）と呼ばれる。例えば**図2**のように、断裂した末梢神経を生体吸収性チューブでつなぐことで、ある期間、末梢神経が再生する空間を確保することが目的である。その他、GTRは、歯周組織や顎堤への検討が進んでいる。また、**図1の④**に示した細胞移植は、マトリックスを利用することなく、幹細胞や体細胞などを欠損部位に注入する方法である。臨床という意味で最も進んでいるのが、この細胞移植ではないだろうか。特に自己幹細胞を移植することによる心疾患[4]やバージャー病[5]の治療において優れた効果が報告されている。これらの先進的手法が、一般的な治療法となるには解決しなくてはならない課題もまだまだ多い。我々は、再生医療を支援するあらゆる工学技術の開発を目指して、PLAを一成分とする共重合体からなる機能性スキャホールドの開発、*in vitro* 組織再生を進める新規バイオリアクターの設計開発、細胞の移植効率を向上させるインジェクタブルスキャホールドの開発、さらには、移植細胞を生体内で追跡する分子イメージングシステムの構築などを進めてきた。

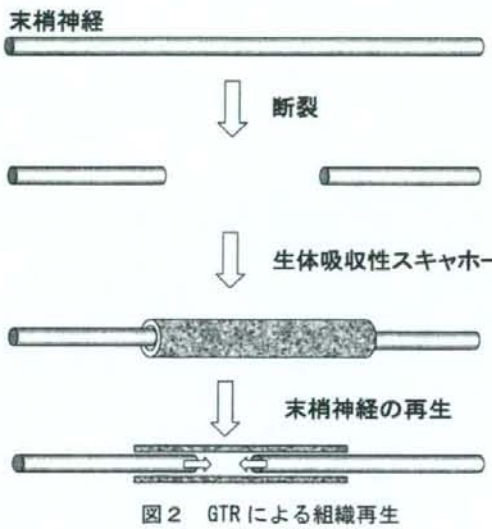

図2　GTRによる組織再生

Ⅲ. ポリ乳酸の化学修飾（柔軟性と細胞特異性）

初期の組織工学では、PGAやPLAなどからなる不織布が採用された。その役割は、文字通り“足場”としての機能であり、細胞が接着して増殖するための固相表面を提供することである。選択された最大の理由は、骨固定ピン[6,7]や外科用縫合糸として既に臨床の場で用いられ、歴史的にも安全性が確保されているためである（**図3**）[8,9]。**図4**には、代表的

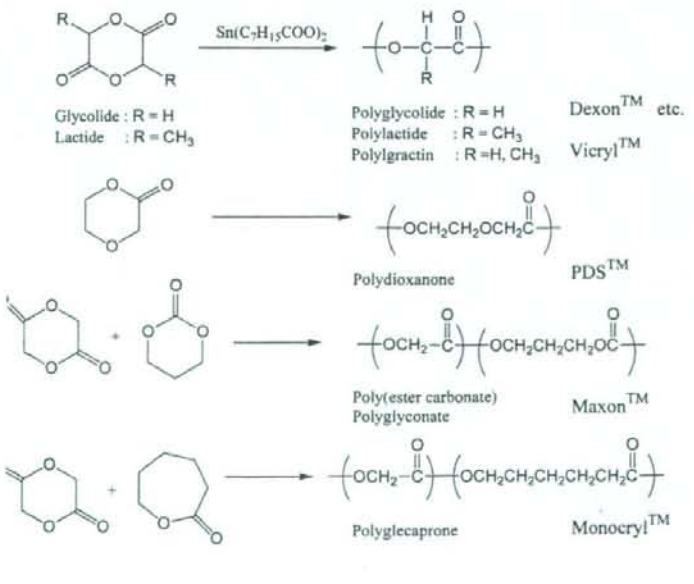

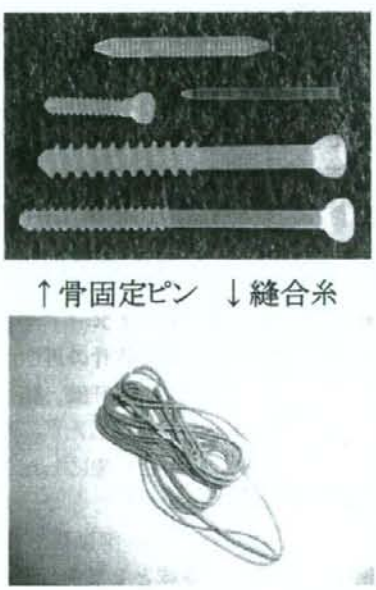

↑骨固定ピン　↓縫合糸

図3　医療用に用いられているポリ－α－ヒドロキシ酸

基　礎　医　学
「再生医療における工学技術」

国立循環器病センター研究所　生体工学部

山　岡　哲　二

Ⅰ．はじめに

近年、ES細胞やさまざまな組織幹細胞の単離に続いて、iPS細胞の作製も報告され、その分化や増殖に関する生化学的・細胞生物学的、あるいは、分子生物学的進歩はめざましい。一方、これらの有用細胞を如何にして組織や臓器へと導くか、あるいは、安全性が担保された臨床システムとして構築するかなど、再生医療における工学サイドのブレークスルーが急務である。

Ⅱ．再生医療

1988年、米国のシンポジウムのタイトルとしてTissue Engineering（組織工学）という用語が初めて使用された[1]。自然治癒が不可能なほど大きな損傷を受けた組織や臓器を修復する試みは古くから行われているが、従来の人工臓器では、材料に対する生体反応の制御が不十分なために長期の機能代替は困難であり、また、臓器移植では、ドナーの不足や免疫応答による拒絶反応に加えて倫理的な問題が残っている。そこで、組織工学の検討が始まり、1993年、R. Langerらは、スキャホールド(Scaffold, 足場材料)と呼ばれたポリグリコール酸（PGA）の不織布に軟骨細胞を播種してヌードマウスの皮下に埋入することで、異所的な軟骨の再生が誘導できること、さらに、この手法が、肝臓、腸、尿管、骨などへ展開できる可能性を示唆した[2]。再生が困難と考えられていた軟骨組織を対象にしたことや、異所的な組織の再構築に成功したことで、世界的に組織工学が注目を集めた。1996年以降、我が国では“再生医工学”という領域として発展した。最近では、その訳語である“Regenerative Medicine”が、海外でも一般的な用語となっている。

実は、このような、マトリックと細胞とを融合させるアイデアは、1980年頃から皮膚組織の再建をターゲットにして検討されていた。フィーダーレイヤー（Feeder Layer）なる細胞層の上で表皮組織が重層化することを利用して表皮シートが作製され、続いて、真皮の再生や、コラーゲンゲルと線維芽細胞、表皮細胞を組み合わせた皮膚の再生が相次いで報告された。その後、上述の軟骨再生へと展開され、さらに1988年には、ヒト胚性幹細胞の単離が報告され[3]、その後も続々と組織幹細胞が、そして、最近、ヒトiPS細胞の作製が報告されるなど、組織工学の最大の問題であった有用細胞の入手問題が解決するとの期待がふくらみ、さらに精力的な研究が進められている。

ますます広がる再生医療研究を内容的に整理すると図1にようになる。まず、再生医工学と細胞移植に大別される。再生医工学の中心は、生分解性マトリックス（スキャホールド）に細胞を播種して組織再生を狙うタイプの戦略である（図1－②，③）。

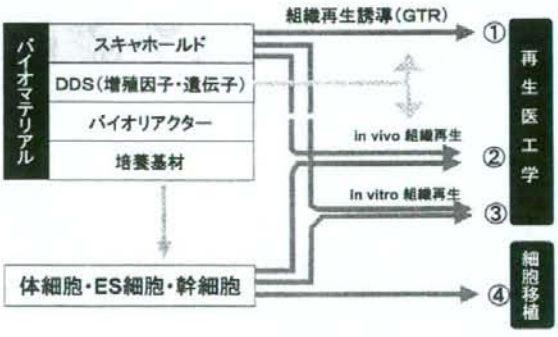

図1　再生医療の戦略

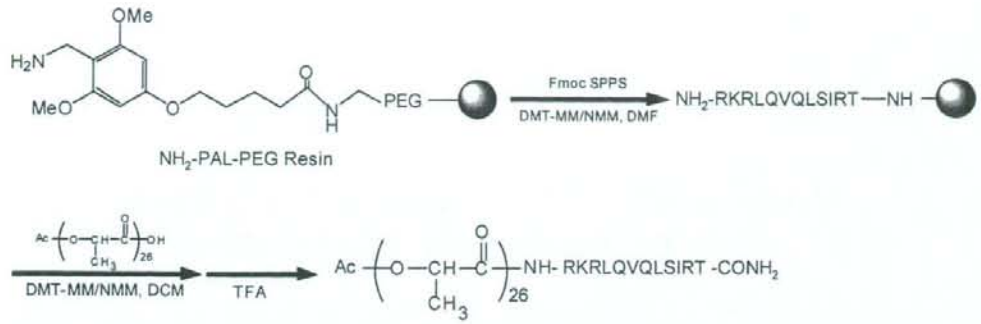

Scheme 1. Synthesis of Ac-OLA26-AG73.

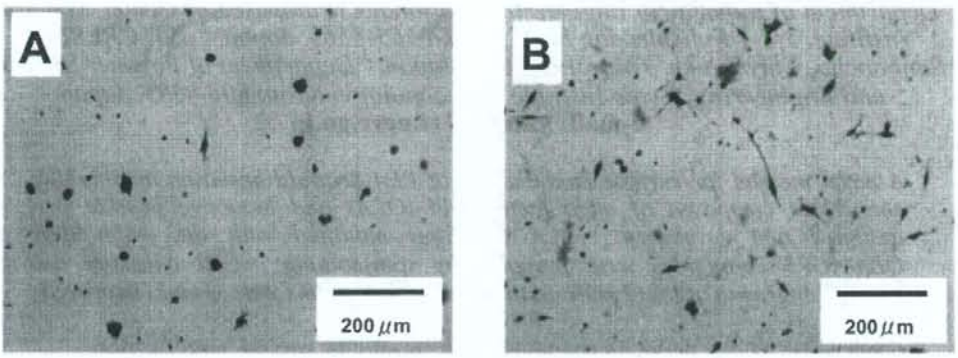

Figure 1. Neurite outgrowth of PC12 cells on PLA (A) and PLA/OLA-AG73 (B) thin-films.

Three weight % of OLA-AG73 conjugates were added to 10 weight % of PLA solution in hexafluoro isopropanol, and the mixed solutions were spin coated onto cover glass (φ 14 mm) or electro spun to aluminum foil, resulting in surface modified thin-films and nano-fiber sheets respectively. As is shown in Figure 1, the cell adhesion and neurite outgrowth of PC12 cells on PLA/OLA-AG73 thin-film were improved and reached to longitudinal and transversal respectively. These behaviors must be resulted from AG73 peptides immobilized on thin-film surface but other factors may also affect it. The physicochemical characteristics should be changed even when only 3 % of OLA-AG73 was added. In addition, the surface density of OLA-AG73 on thin-film and its releasing profiles should be analyzed in detail.

In general nano-stractured PLA scaffolds are much more difficult to be modified than the bulk materials because they are very weak and fragile against to mechanical stress, chemical reaction, and thermal treatment. The newly developed OLA-Peptide conjugates were found to be very powerful tool for modifying such ultra thin-films or nano-fibers just by adding only 3 % to the dope before processing.

References

1. Fujiwara T., Mukose T., Yamaoka, T., Yamane H., Sakurai S., Kimura Y. (2001) *Macromol. Biosci.*, **1**, 204-208.
2. Weeks B. S., Nomizu M., Ramachandran R.S., Yamada Y., Kleinman H. K. (1998) *Exp. Cell Res.*, **243**, 375-382.

Peptide Science 2008: M. Nomizu (Ed.)
The Japanese Peptide Society (2009)

Modification of PLA Scaffolds Using Bioactive Peptide-Oligo (Lactic Acid) Conjugates

Sachiro Kakinoki[1,2], Sho Uchida[1,3], Tomo Ehashi[1,2], Akira Murakami[3], and Tetsuji Yamaoka[1,2]

[1] Department of Biomedical Engineering, National Cardiovascular Center Research Institute, 5-7-1 Fujishirodai, Suita, Osaka 565-8565, Japan, [2] JST, CREST, 5 Sanbancho, Chiyoda-ku, Tokyo 102-0075, Japan, [3] Department of Polymer Science and Engineering, Kyoto Institute of Technology, Kyoto 606-8585, Japan.
e-mail: yamtet@ri.ncvc.go.jp

A novel method for surface modification of PLA scaffold based on amphiphilic conjugates composed of oligo lactic acid (OLA) and bioactive peptide was designed and developed. PLA thin-films modified with the amphiphilic OLA-AG73 conjugates were prepared by spin-coating. Cell adhesion and neurite outgrowth of PC12 cells on the modified thin-films were greatly improved.

Keywords: AG73, nerve regeneration, PLA, scaffolds, surface modification

Introduction

Tissue engineering has been proposed as an approach to create tissues and organs by use of various scaffolds as a temporary extra-cellular matrix. Poly (lactic acid) (PLA) is a preferred biodegradable material since it is non-enzymatically hydrolyzed to low-toxic lactic acid *in vivo* and has high mechanical properties and excellent shaping and molding properties.

On the other hand, PLA has no specific bioactivities and then is preferred to be modified with bioactive molecules. A variety of bioactive peptides has been reported to be useful for tissue regeneration so far. For example, RGD sequence isolated from fibronectin is well known to support cell adhesion. Various modification techniques for PLA which has no functional groups have been proposed [1] but they are quite hard to apply to the nano-stractured PLA scaffold since they are very fragile. In this report, we developed amphiphilic conjugates composed of bioactive peptides and oligo (lactic acid) (OLA) to functionalize nano-stractured PLA scaffolds and evaluate their bioactivities.

Results and Discussion

Bioactive sequence, RKRLQVQLSIRT (AG73) [2], which has been reported to accelerate the neurite outgrowth *in vitro* was selected. OLA whose hydroxyl group end is capped with acetyl group was synthesized by condensation reaction. The OLA-AG73 conjugates were synthesized by Fmoc solid phase procedure (Scheme 1).

in a side-by-side manner. Accordingly, it is well-known that molecular interaction between PLLA and PDLA chains is strong, leading to higher melting temperature. Such molecular arrangement may suppress the hydrolysis of molecular chains in vivo. Thus, the stereocomplexed nanofiber morphology is retained. As a result, inflammatory reaction is limited at the vicinity of the interfacial region between nanofiber mats and the surrounding tissues.

General Discussion. Physiological response of tissues against implanted foreign materials is one of the most significant subjects to be considered in the development of medical biomaterials. In the case of polymeric biomaterials, the degree of the tissue responses, such as inflammatory reactions, partly depends on the chemical structure and, as a consequence, surface hydrophilic nature of the polymers.[23] Additionally, for biodegradable polymers, the degree of tissue responses is affected by the degradability in vivo.[24] For example, poly(glycolic acid) that undergoes degradation in vivo generally in 2−4 weeks is known to cause acute inflammatory reaction as the degradation proceeds.[25] It is known that the hydrolysis by body fluids is the major mechanism contributing in vivo degradation of polymeric biomaterials. We have already shown that the degradation behavior of poly(hydroxyalkanoate)s (PHAs) in vivo are largely affected by the monomer composition.[26] Nanofiber scaffolds made from these PHAs, ranging from poly[(*R*)-3-hydroxybutyrate] to poly[(*R*)-3-hydroxybutyrate-*co*-97 mol %-4-hydroxybutyrate] lead to contrasted tissue responses. The tissue responses were well correlated with the degradability of each polymer scaffolds. The present study using nanofibers of PLLA and stereocomplexed PLA suggested the correlation between the degree of inflammatory reaction in vivo and the change in the bulk size of each nanofiber mats. The changes in bulk size of the nanofibers were correlated to the changes in the microscopic morphology, crystallinity, and molecular weight. All these factors give evidence that the stereocomplexed PLA nanofibers are more stable and thus provoke lower degree of inflammation in vivo than the PLLA nanofibers.

In general, inflammatory reaction is favored in the case where healing occurs in a short period of time. For example, inflammatory reaction stimulates and accelerates the regeneration of some kinds of epithelial tissues. On the other hand, in the case where healing requires a longer time, chronic inflammatory response is not favored. For example, suppression of the inflammatory responses against artificial vessel has significance for treatment of the circulatory organs that requires a period of more than half a year. From this viewpoint, our results show that the stereocomplexed PLA nanofibers are suitable for the purposes where the chronic inflammatory reaction should be avoided, for example, guided nerve regeneration or blood vessel augmentation. On the other hand, conventional PLLA nanofibers may be suitable for the rapidly bioresorbable materials, for example, wound healing patches. Such versatility of the biodegradability would expand the potential of PLAs as biomaterials.

Conclusion

Fiber morphology, crystallinity, and molecular weight of PLLA and stereocomplexed PLA nanofibers before and after implantation in vivo were investigated using SEM, WAXD, and GPC. The stereocomplexed PLA nanofiber retained its fiber morphology, crystallinity, and molecular weight after a 12 week implantation. On the other hand, the PLLA nanofiber showed breakdown of the fiber morphology and significant decrease in crystallinity and molecular weight. The degree of inflammatory reaction against the nanofibers in vivo was correlated to the degradation behavior. The larger stability against hydrolysis of stereocomplexed PLA nanofiber, attributed to the strong interaction between PLLA and PDLA chains in the nanofiber, was confirmed by in vitro degradation.

Acknowledgment. This work has been supported by a grant provided for Ecomolecular Research II in RIKEN Institute (The Institute of Physical and Chemical Research), Japan, and by a Grant-in-Aid from the Ministry of Education, Culture, Sports, Science and Technology, Japan (No. 19350075, to T.I.). We thank Ms. Noreen Fundador for the English correction of our manuscript.

References and Notes

(1) Langer, R.; Vacanti, J. P. *Science* **1993**, *260*, 920–926.
(2) Reneker, D. H.; Chun, I. *Nanotechnology* **1996**, *7*, 216–223.
(3) Morota, K.; Matsumoto, K.; Mizukoshi, T.; Konosu, Y.; Minagawa, M.; Tanioka, A.; Yamagata, Y.; Inoue, K. *J. Colloid Interface Sci.* **2004**, *279*, 484–492.
(4) Murugan, R.; Ramakrishna, S. *Tissue Eng.* **2006**, *12*, 435–447.
(5) Buchko, C. J.; Chen, L. C.; Shen, Y.; Martin, D. C. *Polymer* **1999**, *40*, 7397–7407.
(6) Zong, X.; Kim, K.; Fang, D.; Ran, S.; Hsiao, B. S.; Chu, B. *Polymer* **2002**, *43*, 4403–4412.
(7) Zong, X.; Ran, S.; Kim, K.-S.; Fang, D.; Hsiao, B.; Chu, B. *Biomacromolecules* **2003**, *4*, 416–423.
(8) Ikada, Y.; Tsuji, H. *Macromol. Rapid Commun.* **2000**, *21*, 117–132.
(9) Iwata, T.; Doi, Y. *Sen'i Gakkaishi* **2001**, *57*, 172–177.
(10) Ikada, Y.; Jamshidi, K.; Tsuji, H.; Hyon, S. H. *Macromolecules* **1987**, *20*, 904–906.
(11) Tsuji, H. *Macromol. Biosci.* **2005**, *5*, 569–597.
(12) Okihara, T.; Tsuji, M.; Kawaguchi, A.; Katayama, K.; Tsuji, H.; Hyon, S. H.; Ikada, Y. *J. Macromol. Sci., Part B: Phys.* **1991**, *30*, 119–140.
(13) Tsuji, H. *Polymer* **2000**, *41*, 3621–3630.
(14) Tsuji, H.; Suzuki, M. *Sen'I Gakkaishi* **2001**, *57*, 198–202.
(15) Tsuji, H.; Miyaushi, S. *Biomacromolecules* **2001**, *2*, 597–604.
(16) Takasaki, M.; Ito, H.; Kikutani, T. *J. Macromol. Sci., Part B: Phys.* **2003**, *42*, 57–73.
(17) Furuhashi, Y.; Kimura, Y.; Yamane, H. *J. Polym. Sci., Part B: Polym. Phys.* **2007**, *45*, 218–228.
(18) Tsuji, H.; Nakano, M.; Hashimoto, M.; Takashima, K.; Katsura, S.; Mizuno, A. *Biomacromolecules* **2006**, *7*, 3316–3320.
(19) Ishii, D.; Lee, W.-K.; Kasuya, K.-I.; Iwata, T. *J. Biotechnol.* **2007**, *132*, 318–324.
(20) Kim, K.; Yu, M.; Zong, X.; Chiu, J.; Fang, D.; Seo, Y.-S.; Hsiao, B. S.; Chu, B.; Hadjiargyrou, M. *Biomaterials* **2003**, *24*, 4977–4985.
(21) Zeng, J.; Chen, X.; Liang, Q.; Xu, X.; Jing, X. *Macromol. Biosci.* **2004**, *4*, 1118–1125.
(22) You, Y.; Min, B.-M.; Lee, S. J.; Lee, T. S.; Park, W. H. *J. Appl. Polym. Sci.* **2005**, *95*, 193–200.
(23) Wang, Y.-X.; Robertson, J. L.; Spillman, W. B.; Claus, R. O. *Pharm. Res.* **2004**, *21*, 1362–1373.
(24) Hasirci, V.; Lewandrowski, K.; Gresser, J. D.; Wise, D. L.; Trantolo, D. J. *J. Biotechnol.* **2001**, *86*, 135–150.
(25) Ceonzo, K.; Gaynor, A.; Shaffer, L.; Kojima, K.; Vacanti, C. A.; Stahl, G. A. *Tissue Eng.* **2006**, *12*, 301–308.
(26) Tan, H. Y.; Ishii, D.; Mahara, A.; Murakami, S.; Yamaoka, T.; Sudesh, K.; Samian, R.; Fujita, M.; Maeda, M.; Iwata, T. *Biomaterials* **2008**, *29*, 1307–1317.

BM8009363

Table 1. Number-Averaged Molecular Weight (M_n) and Polydispersity Index (M_w/M_n) of Original PLLA and PLA Nanofibers[a]

	PLLA		PDLA		stereocomplexed PLA	
	M_n	M_w/M_n	M_n	M_w/M_n	M_n	M_w/M_n
original	4.7×10^5	1.8	2.2×10^5	1.5		
nanofiber before implantation	3.8×10^5	2.3			8.7×10^4	3.3
after 4 weeks of implantation	3.0×10^5	2.4			8.6×10^4	2.3
after 12 weeks of implantation	1.7×10^5	2.3			[b]	[b]

[a] PLLA and stereocomplexed PLA before and after 4 weeks and 12 weeks of implantation. [b] Not obtained due to the poor solubility in chloroform.

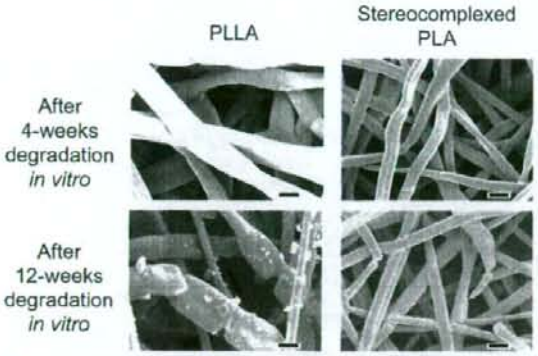

Figure 7. SEM images of PLLA (left) and stereocomplexed PLA (right) nanofibers after 4 weeks (upper) and 12 weeks (lower) in vitro degradation in PBS. Scale bars = 1 μm.

after in vitro incubation showed a considerable increase in the fiber diameter. This suggests that the significant swelling of the nanofibers occurred during the incubation. Interestingly, the stereocomplexed PLA nanofiber showed a smaller degree of swelling (from 300 to 600 nm) than the PLLA nanofiber (from 300 to 1200 nm). Because strong interaction works between molecular chains of PLLA and PDLA in the sterecomplexed PLA nanofiber, the swelling of the stereocomplexed PLA nanofiber might be suppressed.

GPC data of the nanofibers before and after in vitro degradation were also obtained, as shown in Figure 6b. The M_n and M_w/M_n estimated from the GPC curves are listed in Table 2. The M_n of stereocomplexed PLA was almost unchanged while that of PLLA showed a decrease from 3.8×10^5 to 1.8×10^5. These trends are consistent with the molecular weight data before and after the implantation in vivo as shown in Table 1.

The difference in the swelling behavior and molecular weight change in vitro between the stereocomplexed PLA and PLLA nanofibers may explain the results of the subcutaneous implantation in vivo in which the stereocomplexed PLA nanofiber showed smaller degree of absorption than the PLLA nanofiber.

Discussion

Degradation Mechanism of PLLA and Stereocomplexed PLA Nanofibers In Vivo. A schematic representation of the degradation mechanism of the PLLA and stereocomplexed PLA nanofibers is shown in Figure 8. For the PLLA nanofiber, it is believed that the molecular chains in the amorphous region between lamella crystals are preferentially hydrolyzed due to the intracrystalline swelling. This leads to the cleavage of a nanofiber and a decrease in the molecular weight. Then the chain-end degradation at the edge of the cleaved nanofiber may occur and lead to the decrease in the crystallinity. The cleavage of nanofiber may facilitate the delamination and the subsequent fragmentation of the nanofiber mats and, consequently, the

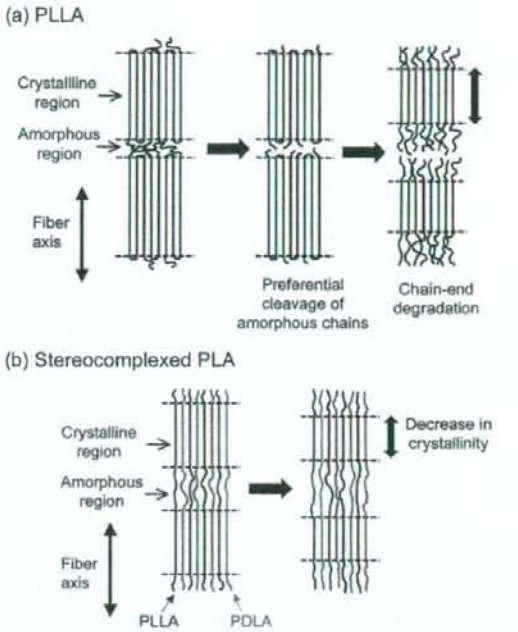

Figure 8. Schematic representation of the structural changes of (a) PLLA nanofiber and (b) stereocomplexed PLA nanofiber during implantation in vivo. For PLLA nanofiber, the amorphous chains between lamella crystals are preferentially hydrolyzed, leading to the cleavage of the nanofiber. Then, the chain-end degradation occurs at the edge of the cleaved nanofiber. Crystallinity of the PLLA nanofiber is thus considerably lowered. In contrast, degradation of stereocomplexed PLA is suppressed by the strong interaction between PLLA and PDLA chains, although the crystallinity slightly decreases.

Table 2. Number-Averaged Molecular Weight (M_n) and Polydispersity Index (M_w/M_n) of PLLA and Stereocomplexed PLA Nanofibers[a]

	PLLA		stereocomplexed PLA	
	M_n	M_w/M_n	M_n	M_w/M_n
before degradation	3.8×10^5	2.3	8.7×10^4	3.3
after 4 weeks of degradation	1.4×10^5	3.5	8.4×10^4	3.0
after 12 weeks of degradation	1.8×10^5	3.0	6.9×10^4	2.2

[a] Before and after 4 weeks and 12 weeks of degradation in vitro.

infiltration of surrounding tissues in the PLLA nanofiber mat. Inflammatory reaction at the early stage may be due to the acidic low-molecular-weight degradation products and fragmented nanofibers.

A different situation was observed for the stereocomplexed PLA nanofibers. It is supposed that a single stereocomplexed PLA nanofiber is composed of PLLA and PDLA chains aligned

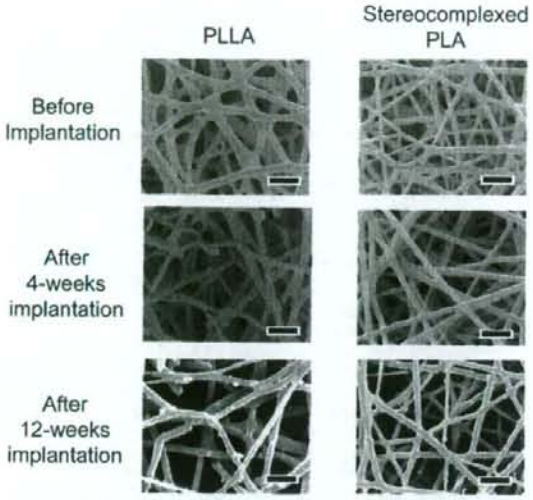

Figure 4. SEM images of PLLA (left) and stereocomplexed PLA (right) nanofibers. Upper row, before implantation; middle row, after 4 weeks of implantation; lower row, after 12 weeks of implantation. The surrounding tissues were removed by trypsin treatment. Scale bars = 1 μm.

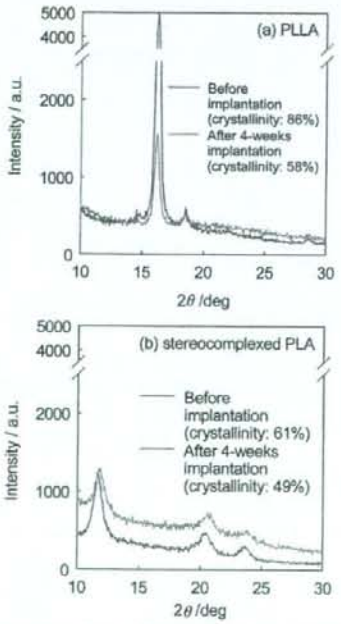

Figure 5. Wide-angle X-ray diffraction patterns of PLLA and stereocomplexed nanofibers before and after 4 weeks of implantation. PLLA nanofiber showed diffraction peaks at 2θ = 15.1°, 16.5°, and 18.1° that are assigned to homopolymer crystal of PLLA. On the other hand, stereocomplexed PLA nanofiber showed diffraction peaks at 2θ = 12.0, 20.8, and 24.1° that are assigned to stereocomplexed crystal. No diffraction peaks assigned to homopolymer crystal were observed in stereocomplexed PLA nanofiber.

Changes in Crystallinity. Figure 5 shows the WAXD patterns of the PLLA and stereocomplexed PLA nanofibers before and after 4 weeks of implantation. While the PLLA nanofiber showed diffractions that are assigned to the α-form crystal of PLA, the stereocomplexed PLA nanofiber showed diffractions assigned only to stereocomplexed crystal.[12] The crystallinity of both nanofibers was calculated as the ratio between the integrals of crystalline diffraction intensity and the total diffraction intensity. While the PLLA nanofiber showed considerable decrease in its crystallinity from 86 to 58%, the stereocomplexed PLA nanofiber showed a smaller decrease from 61 to 49%. These results show that the crystallinity of the stereocomplexed PLA is not so much lowered by implantation, while that of PLLA nanofiber significantly decreases. These results support the higher stability of stereocomplexed PLA nanofiber than PLLA nanofiber, as seen from visual inspection of the explanted nanofiber mat and the histological observation.

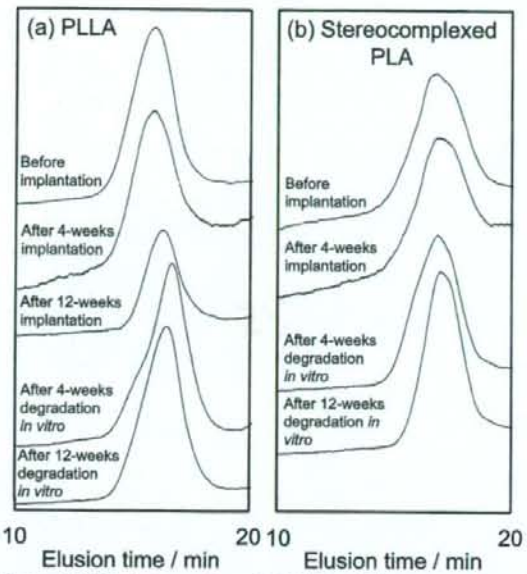

Figure 6. GPC elusion profiles of (a) PLLA and (b) stereocomplexed PLA nanofibers before and after implantation in vivo for 4 weeks and 12 weeks and before and after in vitro degradation for 4 weeks and 12 weeks.

GPC Analysis. The possibility of the cleavage of molecular chains during implantation, as suggested from SEM and WAXD data, was investigated by GPC analysis. The GPC elusion profiles are shown in Figure 6. Table 1 shows the number-averaged molecular weight, M_n, and the polydispersity index, M_w/M_n, of the PLLA and stereocomplexed PLA nanofibers before and after 4 weeks of implantation. Data for original PLLA are slso shown in Table 1. In the case of 12 weeks, GPC data of stereocomplexed PLA were not obtained because of its low solubility in chloroform. PLLA nanofiber showed a decrease in M_n during the implantation. In contrast, the M_n of stereocomplexed PLA nanofiber remained unchanged despite the decrease in M_w/M_n for 4 weeks of implantation. These results indicate that stereocomplexed PLA was not degradaded during implantation, while the PLLA chains in the nanofiber were considerably degraded. Additionally, in the case of the stereocomplexed PLA nanofiber, the extraction of low molecular weight fraction might occur during implantation.

In Vitro Degradation. To consider the results obtained from the in vivo experiment in terms of biocompatibility and bioabsorption, changes in the structure and properties of the nanofibers after in vitro incubation were investigated. As seen in Figure 7, both PLLA and stereocomplexed PLA nanofibers